Polarization Measurement of Proton Beam at 185 GeV by the Coulomb Coherent Process

AUTHOR(S):

Nagamine, Tadashi

CITATION:

Nagamine, Tadashi. Polarization Measurement of Proton Beam at 185 GeV by the Coulomb Coherent Process. Memoirs of the Faculty of Science, Kyoto University. Series of physics, astrophysics, geophysics and chemistry 1990, 38(1): 69-94

ISSUE DATE:

1990-03

URL:

http://hdl.handle.net/2433/257614

Memoirs of the Faculty of Science, Kyoto University, Series of Physics, Astrophysics, Geophysics and Chemistry, Vol. XXXVIII, No. 1, Article 3, 1990

Polarization Measurement of Proton Beam at 185 GeV by the Coulomb Coherent Process

By

Tadashi NAGAMINE

Department of Physics Faculty of Science, Kyoto University

(*Received January 6, 1989*)

Abstract

The polarized proton beam line with the world highest energy has been constructed at Fermi National Accelerator laboratory (FNAL). The polarization of protons was obtained from the parity-violating decay of the Λ^0 particles. The momentum of the beam was approximately 185 GeV/c and the intensity of the beam was about 8×10^6 per spill. The asymmetries of the Coulomb coherent production of the π^0 by the polarized proton beam in the Coulomb field of nuclei were observed for the first time. Both forward scattered proton and π^0 from nuclear targets were detected with the good t-resolution of less than 1×10^{-3} $(\mathrm{GeV/c})^2$, in order to identify the Coulomb coherent production process. The measured asymmetry for the lead target is (0.14 ± 0.03) in the $p\pi^0$ mass region of $1.36\sim1.52\ \mathrm{GeV/c^2}$, $|t|$ of less than 1×10^{-3} $(\mathrm{GeV/c})^2$ and the angular range of $60\sim105$ degree in θ_{GJ}. The polarization of the beam was found to be 0.40 ± 0.90. This value is consistent with the value calculated from the decay asymmetry of the Λ^0-particle. This measurement demonstrates that the Coulomb coherent production can be used for the polarimeter to measure the polarization of protons at high energies.

1. Introduction

Various polarization effects are expected to be observed in hadron-hadron interactions at high energies, such as high-$P_T\pi^0$ production and large-x_F meson productions. There have been several experiments which suggest the large spin effect at high energies. The large asymmetry in the inclusive π^0 production at high-P_T by 24 GeV protons on polarized proton target was observed at CERN.[1] The observed asymmetry increases up to almost 100% as P_T increases to 3 GeV/c. Such an asymmetry was also seen in the inclusive π^0 production in the π^- collision using a 40 GeV π^- beam at Serpukhov.[2] The large asymmetries of meson and hyperon productions at large-x_F were also observed at several incident energies. They have a small energy dependence as predicted by theoretical models. For the further study of spin effects it is indispensable to use very high energy polarized proton beams. Unfortunately, so far, it is difficult to accelerate the polarized proton beam up to the higher energy than 25 GeV.

Recently the polarized proton beam with the world highest energy was constructed at FNAL.[3,4] The polarization of protons was obtained from the parity-violating decay of the Λ^0 particles which were produced inclusively in p-nucleus collision. The beam energy was 185 ± 11 GeV. The typical intensity was 8×10^6 protons for 1×10^{12} primary

protons. The polarization of each proton can be calculated from the decay kinematics of the Λ^0 particle. Since the beam trajectory reflects the decay kinematics, the polarization of each proton is determined from the measurement of the beam trajectory. The track of each proton was measured by the sets of bending magnets and hodoscopes at the mid-point of the beam line. Theoretically, the polarization of each proton can be calculated from the informations of these hodoscopes. Since mis-alignement of these magnets and hodoscopes could affect the calculation of polarization, the polarization obtined by this method must be compared with the measurements by other methods.

The beam polarization was measured by two methods in the experiment. One of them is the measurement on the asymmetry of the coherent production of π^0 in the Coulomb field of the heavy nuclei. The Coulomb coherent production of hadrons was formulated by Primakoff et al., for the measurement of the π^0 life-time for the first time.[5] Since then, it has been an useful tool to study the electro-magnetic properties of particles such as the π^0 life-time, radiative decay widths of various hadrons.[5,6] Since the nucleus plays a role as a point source of the Coulomb field in the formulation, the reaction has characteristics of the photon-hadron reaction at the γ-p vetex. The coherent production in the Coulomb filed of nuclei is related to the photo-production in the lower energy region.[7,8,9] The idea is applicable to the relation between both reaction with polarized particles. Therefore, we can determine the polarization of the beam accurately from the measurement of the asymmetry of the π^0 production in the Coulomb field of the heavy target by the polarized proton beam, by knowing the asymmetry of the π^0-photo-production off the polarized proton target.[7,8] The low-energy π^0-photo-production off polarized proton has a large asymmetry (maximum 0.9) at a photon energy of around 600 MeV,[10,11,12] which corresponds to the $p\pi^0$ mass of about 1.4 GeV/c^2.

In order to identify the Coulomb coherent process, it is necessary to measure the reaction with a t-resolution of less than 10^{-3} (GeV/c)^2.

Another method to measure the beam polarization was the proton-proton elastic scattering in the Coulomb-nuclear interference (CNI) region.[14] The elastic scattering of polarized proton by unpolarized proton at a small momentum transfer squared, $|t|=3\times 10^{-3}$ (GeV/c)^2, has the analyzing power of 5% due to the intererence between the electro-magnetic spin-flip amplitude and nuclear non-flip amplitude. The scattering angle of the proton has to be detected with an angular resolution of 1×10^{-5} radian and the t-resolution of 4×10^{-4} (GeV/c)^2 for 185 GeV protons.

In this report, first we will describe the principle of the Coulomb coherent production in Chapter 2. The production of the polarized proton beam at FNAL will be also mentioned briefly in Chapter 3. Then, Chapter 4 will explain the experimental method. The analysis of the asymmetry measurement on the π^0 production in the Coulomb field of lead and other targets using the polarized beam will be explained in Chapter 5. A comparison will be made between our data and available data on the low energy π^0-photoproduction in order to obtained the beam polarization. The results will be compared with other measurements of the polarization.

2 Coulomb Coherent Production

2.1 Kinematics of the Coherent Production

In this section, the kinematics of the coherent production of π^0 from scattering of polarized protons in the Coulom field of the heavy nucleus illustrated in fig. 1 (a) are discussed. The nucleus Z, such as lead and copper, is assumed to remain in its ground state.

$$p+Z\rightarrow p+\gamma'+Z\rightarrow p+\pi^0+Z. \tag{1}$$

In the coherent scattering, the momentum transfer $\boldsymbol{k}$ to the nucleus is very small, that is $1/R\sim 30\,\mathrm{MeV/c}$ for lead, so that the incident proton interacts with entire nucleus. Therefore, the scattering angle of the $p\pi^0$ system in the laboratory frame is very small for the incident proton energy of about 185 GeV. The relation between the incident proton energy, E_B, and the energy of $p\pi^0$, $E_{p\pi^0}$, can be written as

$$E_B=E_{p\pi^0}+k^2/2M, \tag{2}$$

where M is the mass of the nucleus and k is the momentum transfer. Because the nucleus Z is heavy and k is very small, the energy transfer to the nucleus Z is negligibly small, i.e., $k^2/2M\ll 1$. Then the energies of the incident proton and $p\pi^0$ are almost the same.

$$E_B=E_{p\pi^0}. \tag{3}$$

The relation between the momenta of the incident ptoton and $p\pi^0$ is expressed as

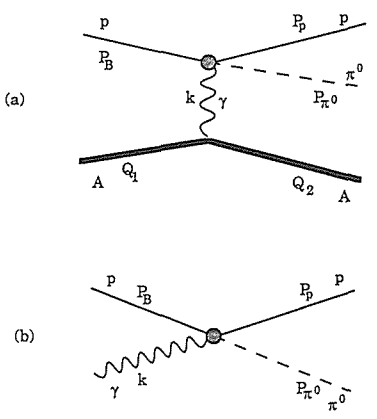

Figure 1 Feynman diagrams of (a) the Coulomb coherent process and (b) the π^0-photoproduction.

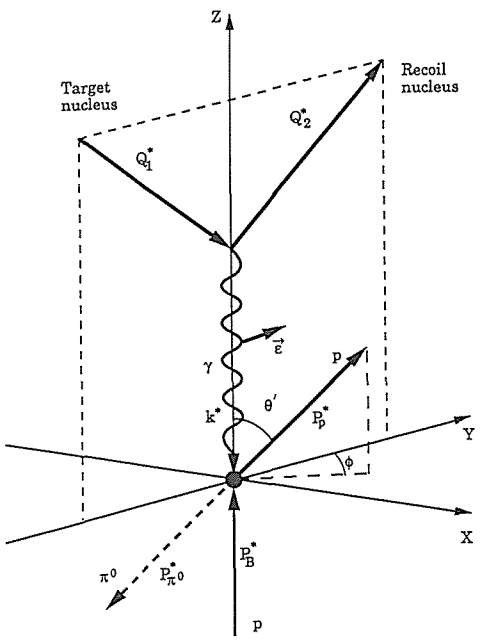

Figure 2 The Coulomb coherent process in the Gottfried-Jackson frame.

$$P_B = P_{p\pi^0} + \Delta P, \tag{4.a}$$

with $$\Delta P = [(m_{p\pi^0})^2 - m_B^2] / 2P_B, \tag{4.b}$$

where ΔP is the minimum momentum transfer, m_B is the proton mass and $m_{p\pi^0}$ is the invariant mass of proton and π^0. The momentum transfer $\boldsymbol{k}$ is

$$\boldsymbol{k} = \boldsymbol{P}_B - \boldsymbol{P}_{p\pi^0} = \boldsymbol{P}_T + \Delta \boldsymbol{P}, \tag{5.a}$$

$$P_T = \theta P_{p\pi^0}, \tag{5.b}$$

where θ is the scattering angle of the $p\pi^0$ system in the laboratory frame and P_T is the transverse momentum of the $p\pi^0$ system.

2.2 Coulomb Coherent Production of the Polarized Proton

The amplitude of the process is written as[9]

$$A = (Q_1 + Q_2)^\mu \frac{Ze}{k^2} J_\mu F(k^2), \tag{6}$$

where $(Q_1 + Q_2)^\mu$ is the nucleus current, Q_1 and Q_2 are four momenta of the nucleus in the intial and final state, respectively. J_μ is a current for $p \to p + \pi^0$, and $F(k^2)$ is the charge form factor of a nucleus. Due to the conservation of the electromagnetic current $k^\mu J_\mu = 0$, the amplitude can be written as

$$A = -\frac{Ze}{k^2} F(k^2) \frac{2M|P_B|}{m|k'|} \varepsilon_T J_T, \tag{7}$$

where m and M are the masses of the protn and nucleus, respectively $|k'|$ is the photon momentum in the C.M.S. of the scattered proton and π^0, and $\varepsilon_T J_T$ is the matrix element for the real photon and proton. The differential cross section of the Coulomb process is

$$\frac{d\sigma}{ds_1 dk^2 dt\, d\phi} = \frac{\pi}{16\lambda(S, m^2, M^2)\lambda^{1/2}(s_1, k^2, m^2)(2\pi)^5} |A|^2, \tag{8}$$

$$S = (P_1 + Q_1)^2,$$

$$s_1 = (m_{p\pi^0})^2,$$

$$\lambda(x, y, z) = x^2 + y^2 + z^2 - 2xy - 2xz - 2yz,$$

where t is a momentum transfer squared between the incident and scattered protons. ϕ is the azimuthal angle of the photon polarization relative to the direction of the scattered proton about the direction the incident proton in the C.M.S. of $p\pi^0$ as shown in fig. 2. Comparing the equation (8) with the differential cross section fo the π^0 photoproduction,

$$\frac{d\sigma(\gamma_\uparrow\, p_\uparrow \to \pi^0 p)}{dt\, d\phi} = \frac{1}{32\pi^2} \frac{1}{\lambda(s_1, m^2, 0)} |\varepsilon_T J_T|^2, \tag{9}$$

the differential cross section of the Coulomb coherent production can be expressed as

$$\frac{d\sigma}{ds_1 dk^2 dt\, d\phi} = \frac{Z^2\alpha}{\pi}\,\frac{P_T^2}{k^4}\,\frac{1}{(s_1-m^2)}|F(k^2)|\frac{d\sigma(\gamma_\uparrow\, p_\uparrow \to \pi^0 p)}{dt\, d\phi}. \tag{10}$$

The cross section of the π^0-photoproduction by the unpolarized photon on the polarized proton can be written as[8,9,10]

$$d\sigma(\gamma\, p_\uparrow \to \pi^0 p) = d\sigma(\theta')\,\{1+T(\theta')s_y\}, \tag{11}$$

where s_y is the y-component of the polarization of the incident proton, $d\sigma(\theta')$ is the unpolarized differential cross section for π^0-photo-production, $T(\theta')$ is the polarized target asymmetry, and θ' is the angle between the target proton and scattered proton in the C.M.S. After integrating the equation (10) over ϕ, the cross section of the Coulomb process for the polarized proton can be written using the equation (11) as

$$\frac{d\sigma}{ds_1 dk^2} = \frac{Z^2\alpha}{\pi}\,\frac{P_T^2}{k^4}\,\frac{1}{(s_1-m^2)}|F(k^2)|^2\, d\sigma(\theta')\,\{1+T(\theta')s_y\}, \tag{12}$$

where θ' is an angle between the incident and scattered protons in the C.M.S. of the scattered proton and π^0. Therefor the analyzing power A_N of the Coulomb process equals to the target asymmetry $T(\theta')$ of the low energy π^0 photoproduction.

There were several measurements on the analyzing power of the π^0-photoproduction. The data[10,11,12] from those experiments on the low energy π^0-photoproduction shows that $T(m_{p\pi^0}, \theta')$ is about 90% at $\theta' \sim 90^\circ$ and $m_{p\pi^0}=1.4$ GeV/c^2 as shown in fig. 3. The useful ranges of θ' and $m_{p\pi^0}$, where $T(m_{p\pi^0}, \theta') \geq 0.5$, are $70^\circ \sim 120^\circ$ and 1.36 GeV/c$^2 \sim$ 1.52 GeV/c^2, respectively.

The cross section of the Coulomb process is calculated by using the equation (12) with the π^0 photoproduction data.[10,11,13] It is approximately 0.5 mb for $m_{p\pi^0}=1.36$ GeV/c$^2 \sim 1.52$ GeV/c^2 and $|t|<0.001$ (GeV/c)^2 including the effect of the resolution of measurement, and it agrees with the data from other experiment.[15-17]

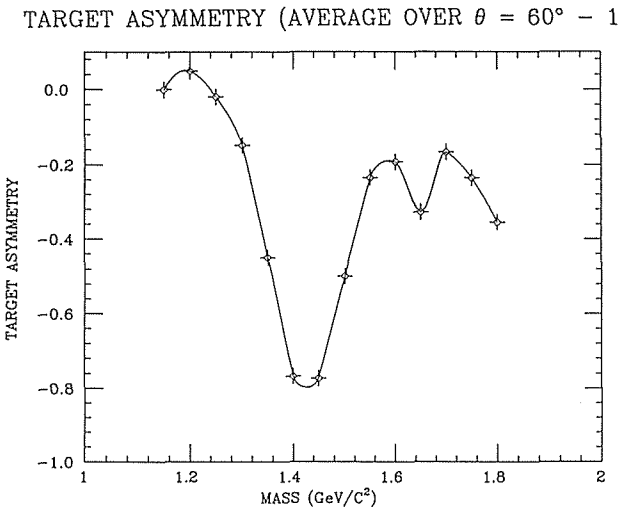

Figure 3 Target asymmetry T of the $\gamma p \to \pi^0 p$ as a function of the invariant mass of $p\pi^0$.

2.4 Background Process from Strong Interaction

The main background of the Coulomb coherent production is the diffractive dissociation. The cross section of the diffractive dissociation is well expressed by an exponential form of exp $(-b_D t)$ for the t-range up to the first minimum. The value of slope parameter of the diffractive process is mostly determined by the radius of the target nucleus.[18–21] For the lead target, the value of slope parameter b_D is approximately 400 $(\mathrm{GeV/c})^2$. The value of slope parameter of the diffractive process is smaller than that of the Coulomb coherent production even with the smearing effect due to the resolutions of the detector. According to the Deck-model, the pion-exchange diagram is dominant over the other diagrams, such as the baryon exchange and direct diagrams (fig. 4).[18–21] The differential cross section of the diffractive process depends on the ϕ_{GJ} (the azimuthal angle of the scattering proton relative to the incident proton in the Gottfried-Jackson frame). The differential cross section has a peak at $\phi_{GJ}=2\pi$.

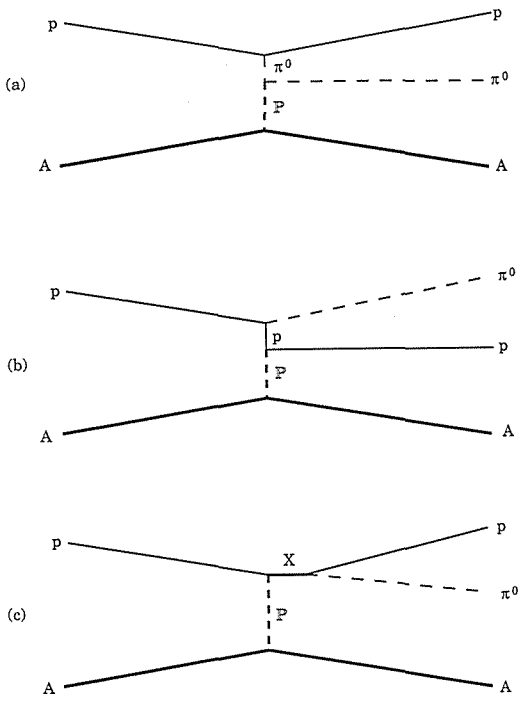

Figure 4 Feynman diagrams of the diffractive process; (a) pion-exchange, (b) proton-exchange, and (c) direct.

3 Polarized Proton Beam at FNAL

3.1 Λ^0 decay as a Polarized Proton Source

The polarized protons was provided from the decay of Λ^0-particle that was produced by the 800 GeV proton beam hitting a Be target of 1.5 mm in thickness, 5.0 mm in hight and 30.0 cm in length. In the rest frame of Λ^0-particle, the proton coming from the parity-violating weak decay is polarized at about 64% along in its momentum for all angle.[22,23] The direction of the spin of the transversely polarized proton is

conserved in the transformation from the C.M.S. to the laboratory frame.

The 800 GeV/c proton beam from the proton synchrotron, TEVATRON, was brought through the primary beam line to the production target for 20 seconds every minutes. Since the production rate of the Λ^0 particles by the 800 GeV protons was high, the resulting intensity of the polarized proton was about 10^7 protons per 10^{12} primary protons. The beam intensities calculated for the 800 GeV and 1000 GeV primary beam energy are shown in fig. 5 as a function of the momentum of the polarized protons and anti-protons. After the production target, the primary protons were swept by the dipole magnets to avoid producing extra particles. Some fraction of Λ^0 particles decayed in flight between the sweeping magnet and first quadrupole magnets of the secondary beam line. The protons coming from the Λ^0 decay were bent downward by the several dipole magnets and the rest of Λ^0 and neutrons were absorbed at the neutral dump. At this point, the momentum of the protons was selected by the vertical collimator, and the momentum bite was $\pm 8\%$ at the central momentum of 185 GeV/c. The contamination of other particles was found to be 15% of the total beam intensity and was detected by the Cherenkov counter in the secondary beam line. The contamination was mostly due to charged π and μ.

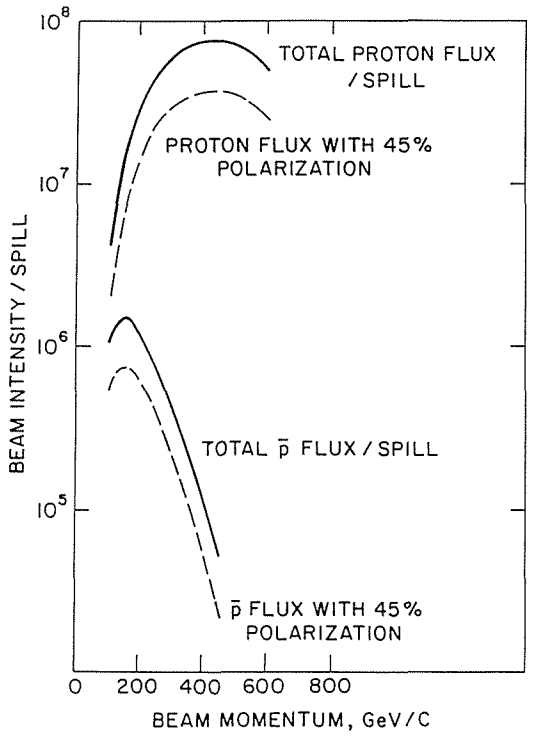

Figure 5 Polarized proton and anti-proton intensity as a function of the momentum for the primary proton beam of 800 GeV/c and 1000 GeV/c with intensity of 3×10^7 protons.

3.2 Polarized Proton Beam Line

The elements in the secondary beam line were carefully designed so that the integrated magnetic field should be zero for both the bending magnets and the focusing quadrupole magnets. This was achieved by configuring the magnets symmetrically as

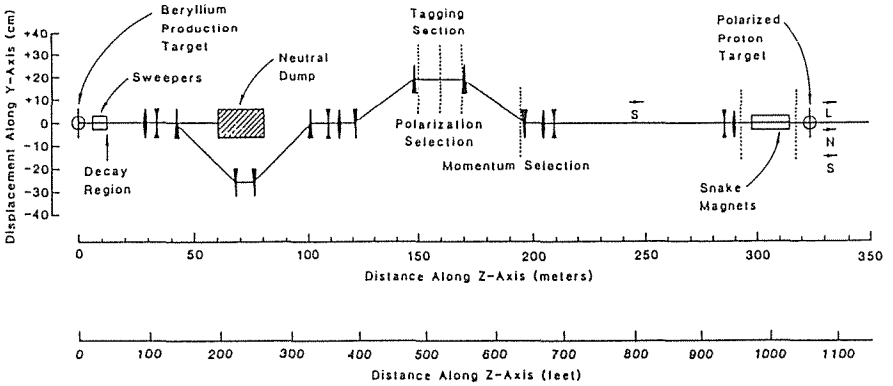

Figure 6 Side view of the polarized proton beam line (MP) at FNAL.

seen in fig. 6. Since the direction of the magnetic fields of all bending magnets were horizontal, the horizontal component of the spin of the polarized proton did not change even if the field integral of the bending magnets was not exactly zero.

The beam was focused at the middle of the beam line as described in the next section, and then at the target point in the experimental hall. At each focal point, the beam size and divergence were the same as those of the production target.

3.3 Beam Tagging System

The tagging system was installed at the mid-point of the beam line as shown in fig. 6[3,4] Since the proton coming from the Λ^0-particle decay is in all directions, the spin direction of the protons should be determined for each particle, otherwise the average polarization is zero. The polarization of each proton can be determined by measuring the decay angle. Extraporating the trajectory of the proton from Λ^0 to the plane of the production target we can define the virtual source. The position of the virtual source relates to the decay angle and then the proton polarization. The distance between the target center and the virtual source is roughly proportional to the proton polarization. In order to measure the position of the virtual source, the beam was focused at the tagging station with a magnification factor of one. The image of the beam at this plane also reflected the decay angle due to the decay kinematics.

The trajectory of the beam was measured by two sets of hodoscopes at the tagging station (fig. 7). The hodoscopes POL1 and POL3 were used to measure the horizontal positions of the track. Since the maximum transverse momentum of the proton from the decay of Λ^0 particles is 100 MeV/c, the maximum angle of protons from the beam is 0.54 mrad for the proton momentum of 185 GeV/c. The radius of the virtual source was about 1.25 cm. As the Λ^0-particle production target was 1.5 mm thickness horizontally, the virtual source was the almost same size of the production target. Therefore the position resolutions of the hodoscopes were required to be 2.0 mm horizontally. The horizontal focal point depended on the beam momentum, the beam momentum was measured by the hodoscopes MOM1, MOM2 and MOM3 with the position resolution of 3.3 mm vertically. The polarization for each proton was determined within 5% and

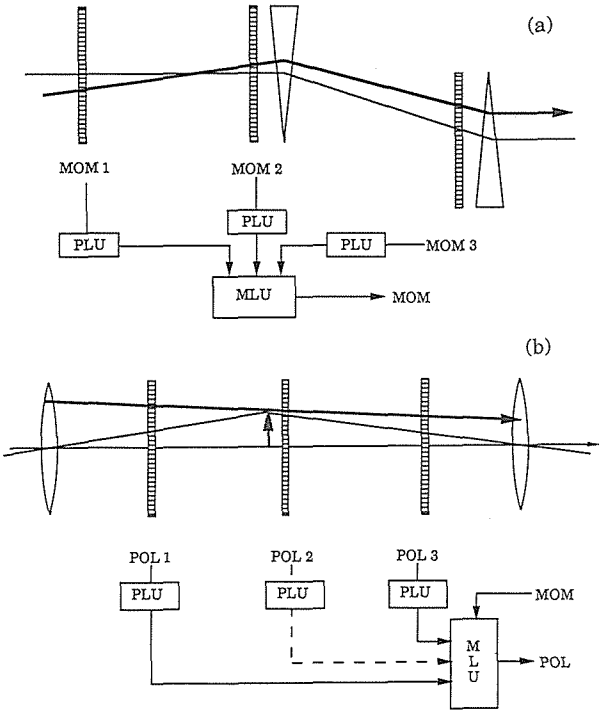

Figure 7 Setup of the tagging hodoscopes and schematic drawing of the associated logic; (a) side view (momentum tagging), (b) top view (polarization tagging).

the momentum resolution was 1.5%.

The information from the hodoscopes were decoded by fast electronics (fig. 7). The signals from the hodoscopes were amplified with gain factors of 10, and digitized by discriminators into narrow digital pulse of 10 nsec wide with the ECL level. Several cascaded programmable matrix logics (PLU) were used to decode the hit pattern into the track information. If the hits could not be resolved as the single hit, the processing did not succeed. Several cascaded memory-look-up units (MLU) were used to calculate the momentum and track position at the focal point from the outputs of the PLU's. The overall processing time was 230 nsec, but the dead time was 60 nsec which was the processing time of the MLU's.

For the diagnostic purpose, the pulse height of the hodoscopes were measured several times during the spill, and some internal latches in the PLU and MLU were read-out at the same time. This information was also used to monitor the beam during the normal data taking runs.

3.4 Snake Magnets

The spin precessing magnets, called a Siberian Snake or Snake magnet,[24] were used to controll the direction of the polarization at the experimental target. The direction of the polarization was reversed periodically in order to reduce systematic errors due to the asymmetric acceptance of the detectors. The vertically polarized proton and longitudinally polarized proton were required for the experiments. Therefore the direction of polarization of the beam, which was horizontal, must be rotated to the vertical or longitudinal direction.

The spin of proton or anti-proton was rotated by a set of magnets with field transverse to the beam direction. The combinations of magnets were chosen to cancel the bends and displacements of the trajectories while leaving a net 90 degree spin precession.

Snake magnets consists of 12 magnets with 45 degree precession each. For example, to tansform the horizontal polarization (S type) to vertical (N type), 8 out of 12 magnets were used. Numbers 3, 5, 6, 7, 8, 9, 10, and 12 of the 12 magnets were used as shown in fig. 8. In order to reverse the final spin direction, only 4 out of the 8 magnets

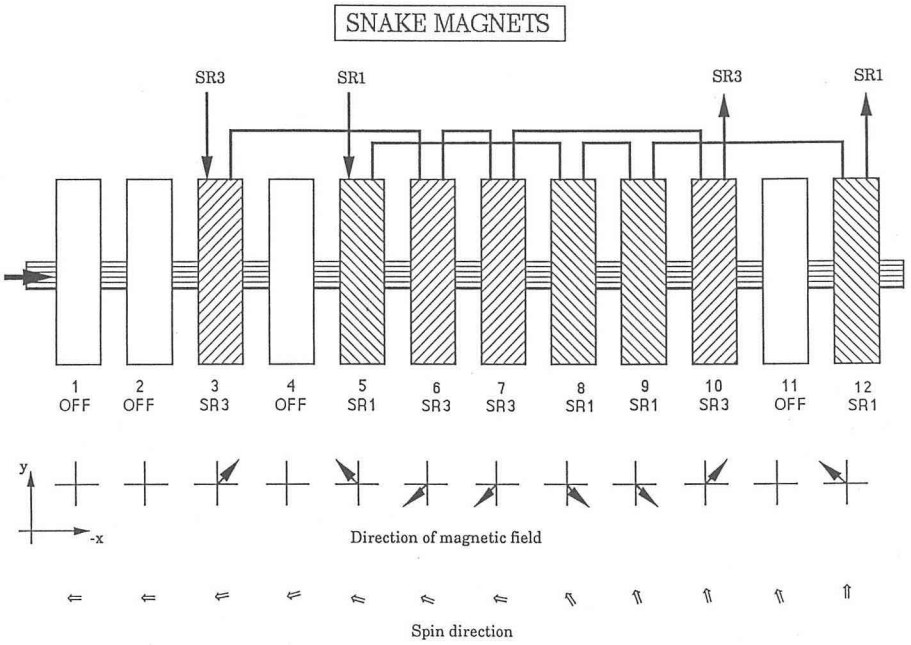

Figure 8 Configuration of Snake magnets and precession of the proton spin.

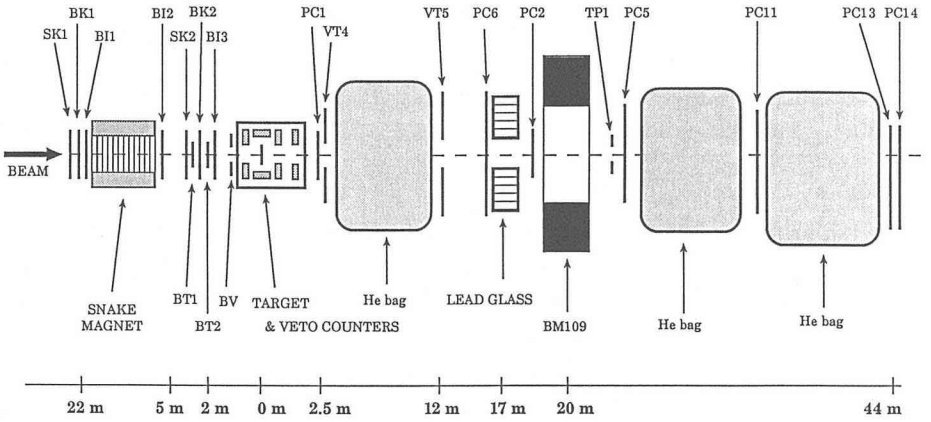

Figure 9 Setup for the Primakoff experiment.

those are 5, 8, 9 and 12 were reversed. Reversing all 8 magnets had no effect on the final spin direction.

4 Experimental Apparatus for the Asymmetry Measurement

4.1 Introduction

The experimental setup is shown in fig. 9. The detector system consisted of the chambers, the proton spectrometer, the π^0-detector and the sets of veto counters. The beam position and angle were measured by five multi wire proportional chambers (MWPC), BK1, BK2, BI1, BI2 and B13, and two sets of hodoscopes, SN1 and SN2. The proton spectrometer consisted of a bending magnet, BM109, three MWPC, PC1, PC6 and PC2, which were placed between the target and the magnet, and four MWPC, PC5, PC11, PC13 and PC14, after the magnet. The lead glass calorimeter was located in front of the magnet to detect the high-energy photons from π^0 decay. The sets of veto counters, VT1, VT2, VT3, VT4 and VT5, were used to reject any inelastic reactions. In addition, the He-bags were installed between the VT4 and VT5, PC5 and PC11, and PC11 and PC13 to reduce the background produced along with the beam line.

4.2 Target and Veto Counters

The target and the veto counters (VT1, VT2 and VT3) were placed on a movable station, that allows to switch from data taking for the Coulomb coherent process to CNI and vice versa quickly. Three kinds of target were used, those are 3 mm thick lead, 5 mm thick copper and 8 cm thick carbon.

The veto counters around the target were used to reject the inelastic reactions. There were two kinds of veto counters. VT1, VT2 and VT3 were for the photons and charged particles and VT4 and VT5 were just for charged particles. The first kind of veto counters consisted of four layers of 6 mm thick lead and the five layers of the 5 mm thick scinitillators in the sandwich structure in the holders made of aluminum of 2 mm thick. The lights emitted from the scintillators were collected by wave-length shifter bars and detected by photomultipliers at the end of the wave-length shifter bars. The wave-length shifter allowed the compact design with a good efficiency for light collection. The typical pulse hight for the minimum ionizing particles was 100 mV at 50 ohm load and the threshold voltage of the discriminators were set at 1/3 of the pulse heights.

Two sets of veto counters for charged particles with a hole at the center (VT4 and VT5) were placed between the target and the lead glass calorimeter. They covered most of the acceptance of the lead glass calorimeter where the gamma veto counter could not cover. The sizes of the holes were large enough for the incident beam and the scattered proton to pass through. The last veto counter (VT5) was placed about 5 m upstream from the lead glass calorimeter in order to reject the scattered particles from lead glasses.

4.3 Beam Chambers

Five MWPC's were used to measure the beam direction. Two MWPC's (BK1 and

BI1) were located upstream of the Snake magnets and three MWPC's (BI2, BK2 and BI3) were between the snake magnets and the target. These MWPC's had X and Y plane and wire spacings were 1 mm. Because the beam line was operated with the rate of more than 10^7 particles/ 20 seconds spill, the beam chambers must work at high intensity of more than 1 MHz. The carbon-cathode MWPC (BK1 and BK2) with 1 mm spacing of sense wires has been developed for this purpose.[25] The effective area of the chambers were 9.6×9.6 cm^2, the gaps between cathode planes and sense wires were 4 mm. The gas mixture for these MWPC's was Ar:Isobutane:Freon=82.56:17.2:0.24, and supplied through bubbler with methylal of 3℃. The MWPCs were operated at 3.7 KV, and the efficiencies were better than 95%. The angular resolution of 2.7×10^{-5} radians for beam tracks was achieved.

4.4 Proton Spectrometer

The trajectories of the scattered protons were measured with PC1, PC6 and PC2, and then the momentum of these protons were measured by using the bending magnet, BM109, and three MWPC's, PC11, PC13 and PC14. The chambers PC1, PC2, PC5 and PC6 consist of four planes (UYXV) giving the redundancy for the reconstruction of tracks. The wire angles of U and V planes were 28.1 and -28.1 degrees from direction of the wire of X plane. The typical operating voltages for these chambers were 4.1 kV for the same gas mixture as used for beam chambers. The efficiency of each plane of these chambers was kept higher than 90% during the data taking runs.

The spectrometer magnet BM109 with the pole-gap of 30 cm and length of 1.94 m, was operated in the ramp mode and the current during spills was 3000 A at a field integral of 2.7 Tesla-meter. The field integral was rather uniform for all the scattered protons. Because of this, the momentum was simply obtained from the bending angle of tracks.

The angular resolutions of the trajectory measurements were 2.9×10^{-5} radian for the scattered protons and the bending angular resolution is 6.4×10^{-5} radian. Since the bending angle of 185 GeV/c proton by the magnet was 4.3×10^{-3} radian, the momentum resolution of this spectrometer was 1.5% for beam particles and better for scattered protons.

4.5 Readout Systems for MWPC

The RMH, PCOS-3 and PCOS-2 systems were used to read out the MWPC's. The RMH system was developed at CERN.[26] The output signals from the amplification and discrimination cards were differential ECL level and were recorded by latch modules. The hit-patterns in the latch modules were encoded into the wire address. The PCOS-3 system and Nanomaker amplifier cards were used for processing the information from BK1, BK2 and PC13. The outputs from the cards were also ECL differential level. The latch module had 32 input channels, and had the internal delay for the signals. The delay time of the modules can be set by the computer through a CAMAC interface.

4.6 Lead Glass Calorimeter

The photons from π^0 decay were detected by the lead glass calorimeter. The

overall size of this detector was 53.5 cm×53.5 cm and it had a hole of 15.3 cm heigh and 15.3 cm wide at the center where the incident and scattered protons passed through as shown in fig. 10. The lead glass blocks and photomultipliers were mounted inside of the soft iron box to shield the counters against to the light, magnetic and electrical fields. The dimension of each block is $3.8\times3.8\times45\text{cm}^3$. Two types of lead glass were used. One of them (F-101) is strong for radiation damage. The radiation length (X_0) of F-101 is 2.36 cm. The length of the block is 19 X_0 and long enough, so that the shower leakage from the end of the lead glass is expected to be less than a few percent. The transparency of F-101 was 60% of the other type of glass (Ohara SF5W). X_0 of SF5W is 2.56 cm and the refractive index is 1.672. They were placed at the outer most layer, because there were less radiation problems (see fig. 10). The light from the lead glass was detected by a 12-stage photomultiplier at the end of the glass. The average operating voltage of these tubes was 1.5 kV. The booster power was supplied to the last four dynodes to improve the linearity and rate dependence of the pulse height. The output signal was 100 mV with the rise of 20 nsec typically for 30 GeV photons.

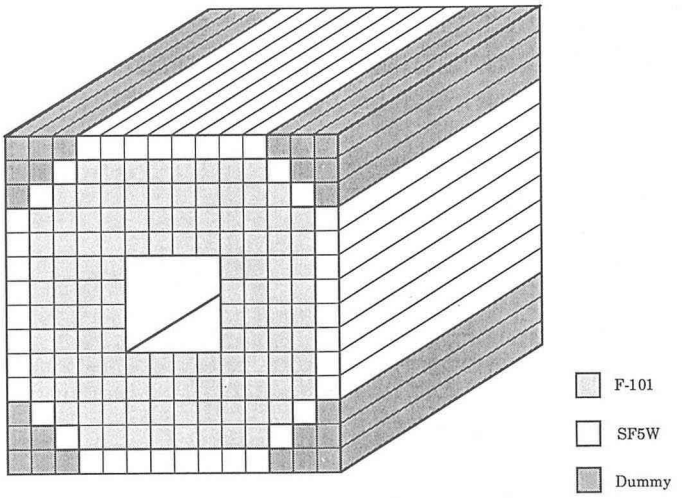

Figure 10 Layout of the lead glass array.

The ADC's of Lecroy's 2280-series were used to digitize the signals from the lead glass calorimeter. The ADC had functions of pedestal subtraction and clustering of adjacent channels. Each module had 24 channels. Its dynamic range was 400 pico Coulomb. The gain was 10 counts/pico Coulomb. The linearities were better than 0.25% for 90% of the dynamic range. The clustering and suppression of small noise signals reduced the readout time. The conversion time of the ADC was 250～350 μsec which was sufficiently fast for our purpose.

The signals from the lead glass were sent to the ADC through the summing amplifiers. 12 summing amplifiers were used, each of which had 16 inputs, 16 though-outputs and 2 sum-outputs. The signals of each input of the summing amplifiers were divided into two with the ratio of 10 to 1, the larger signal was sent to the ADC and small one was sent to the input of the summing amplifier. These were isolated each

other by input transistors, this feature avoided the cross talk among the inputs to be less than 0.1%. These two outputs were also isolated by the transformer to reduce 60 Hz noise from the ground-loop. The gain fluctuation was observed to be less than 1%.

For monitoring the gains of the photomultipliers, the Xe-lamp (Hamamatsu L2360) was used as a light pulsar. The light from the Xe-lamp was delivered to the glasses via optical fibers made of plastic. They were 1 mm in diameter and 1.5 meter in length. The variation of the light transmission among the fibers was found to be less than 10%. The full width of the light pulse was about 1 μsec which was longer than the gate width of the ADC (120 nsec). The gate was set at the peak of the pulse in order to minimize the fluctuation due to the timing. The gate of the ADC was triggered by one of the photomultipliers. In additon to the Xe-lamp, two Am doped NaI crystals were put on the lead glass blocksfor monitoring gains of the photomultipliers. Comparing the Xe-lamp signals and Am-NaI signals, the fluctuation of the Xe-lamp light was monitored.

4.7 Trigger Logic

The trigger logic is shown schematically in fig. 11. The trigger signal was made by the coincidence signal from the sum of energy deposit in the lead glass calorimeter, signals from the beam defining counters and the veto counters. The signals from the lead glass calorimeter were summed partially, up and down, left and right halves. The threshold energies were set to be 25 GeV and 5 GeV typically. The lower threshold was used for the veto of the opposite side half sum. This requirement eliminated a lot of inelastic scattering with a small loss of the signals.

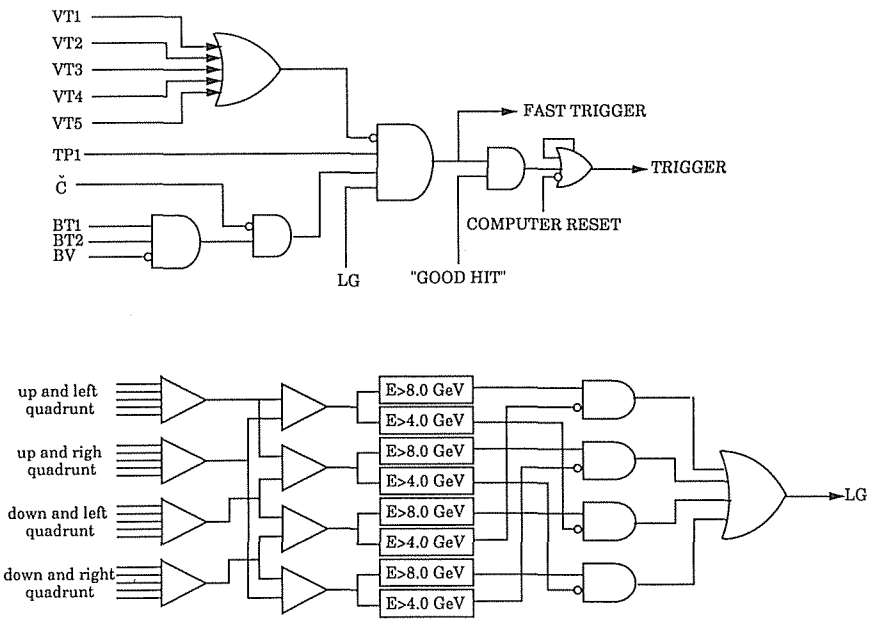

Figure 11 Schematics of trigger logic for Primakoff experiment.

In addition to these, signals from the tagging station were used to make the trigger. The signal from the Cherenkov counter located in beam line was used to reject pions. The "good-hit" signal from the tagging station guaranteed the single particle track in the tagging section.

4.8 Online Computers

Two computers, PDP-11 and VAX11/780, were used for data taking and monitoring. The PDP-11 read the data from CAMAC and wrote the data on the tape. Then the data were sent to VAX11/780 through the DR11W-link which transmitted data at rate of 500K bytes/sec. The online-program on the PDP-11 was based on RSXDA which was developed at FNAL. The rate of data taking with the program was up to 100 Hz for the event size of about 300 of 16-bit words. In addition to data taking, the PDP-11 was also used to control the HV power supplies for the calorimeter photo-tubes, and to set parameters of ADC and PCOS-3. The program on the VAX11/780 executed the reconstruction of π^0, tracks of beam and scattered protons as well as monitoring the efficiencies of the MWPCs and the stability of photo-tubes of the lead glass calorimeter.

The trigger rate during the data taking was 600~800/spill depending on the beam intensity and trigger conditions. Since the average computer dead time was approximately 10 msec, the loss of the beam due to the dead time was 33.4% of the total beam. The dead time due to the FAST triggers for the RMH system was negligibly small compared with the other dead time, because it was less than 1 μsec and 70% of FAST triggers were accepted by the online computers.

5 Data Analysis

Data with the lead target were taken for about 50 hours, and a total number of protons was 1.79×10^{10}. The average beam intensity was $0.5\sim1.0\times10^{7}$ protons/spill. 2.73×10^{6} events were collected with the lead target. Data with the carbon and copper targets were taken for several hours in order to study the diffractive process. Data were also taken without target to study the background events from materials other than the targets. The data for anti-proton beam were taken for 6 hours. But the statistics was not satisfactory to determine the polarization of the anti-proton because the intensity of anti-proton beam was less than 10^{6}/spill.

The data analysis was carried out as the following steps. First the track reconstruction of the incident and scattered protons was performed, and the π^0 reconstruction followed. Then the coherent $p\pi^0$ events was selected. The asymmetries of the coherent process in various kinematical regions were obtained for the selected events. In order to obtain the asymmetry of the Coulomb coherent process, the Coulomb coherent process must be separated from the diffractive process. A ratio of the Coulomb coherent process to the diffractive process was obtained by fitting the t-distribution of the lead target data. The diffractive process was studied with the data of the carbon and copper targets. The each step of the data reduction are described in the following sections.

5.1 Track Reconstruction

The track was basically reconstructed with a single-track finder in three sections. Those are the upstream section from the target, the section between the target and the spectrometer magnet, and the downstream section from the magnet. Then the hit points in each section were fitted with a straight line in order to improve a spatial and angular resolutions of tracks. The beam track was determined by the five MWPC's and two fine segmented hodoscopes (SN1 and SN2). The hodoscopes were useful for finding the track because the detection efficiencies of the track were high. The tracks of scattered protons in the upstream section were reconstructed using PC1, PC6 and PC2. Since there was a leakage of the electromagnetic shower from the lead glass calorimeter, PC2 placed after the lead glass calorimeter had a larger multiplicity than PC6. The tracks of scattereds proton were searched with PC1 and PC6, and the resolution of tracks was improved by use of the PC2 data. The trajectories down stream of the magnet were measured by PC5, PC11, PC13, and PC14. The straight lines obtained from the tracks of scattered protons in the upstream and downstream sections were required to cross in the magnet within the track resolutions.

The reconstruction efficiency of the proton track was found to be about 90%. The momentum resolution is 2% (rms) for the 185 GeV/c proton by comparing with the tagged momentum. "Straight-through" tracks, which were measured without exciting BM109, were used to calibrate the positions of the chambers. The angular resolutions of the incident and scattered proton tracks were 0.02 and 0.03 mrad (rms), respectively. The z coordinate of the interaction point, z-vertex, was reconstructed as the closest point of the incident and scattered proton tracks. The distribution of the z-vertex is shown in fig. 12. This shows that the resolution of z-vertex was 15.7 cm (rms) as expected from the angular resolutions, and the events form the target were well separated from the background events.

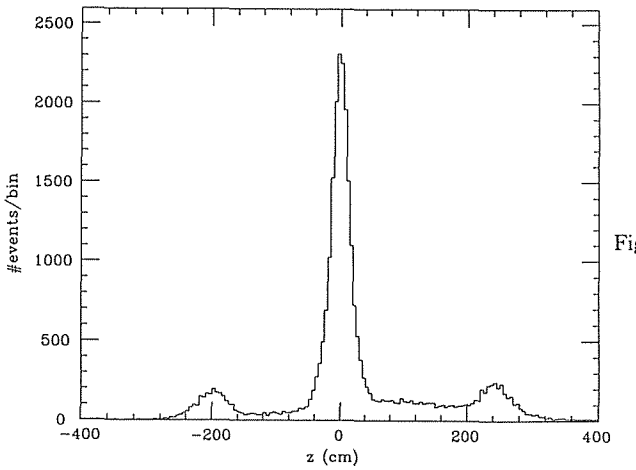

Figure 12 Vertex distribution along the beam direction.

5.2 π^0 Reconstruction

The gain of each block of the lead glass calorimeter was calibrated by using the

electron beam of 28 GeV. The energy resolution of the lead glass calorimeter was found to be 3% at 28 GeV. To reconstruct π^0, the clusters associated to the showers were searched, and the energy and position of the shower were determined. In order to achieve a high efficiency of the reconstruction, we developed the method to reconstruct π^0 in the following cases; (1) the photons hit the inner most blocks of the lead glass calorimeter, (2) the showers of two photons was overlapped because the typical separation of two photons from the π^0 decay was 10 cm. The first problem can be solved by correcting the energy by the known shower profile. However the position of the gamma can not be determined precisely when the photon hits near the wall (1/2 of block). This requires the tight fiducial cut on the photon position. The other problem can be solved by the method described later. This method allowed us to separate two photons which fit two blocks having one module spacing.

The method of finding clusters is as follows; First the block with the maximum energy deposit is searched among all the blocks in which energy deposits are larger than a threshold energy (0.2 GeV) and the block and 8 blocks around it were defined as a cluster. Then the next cluster was searched among the rest of the blocks in the same way. The procedure was repeated until all the the blocks were assigned as member of clusters. A block belonged to several clusters when the showers overlapped. In this case, the energy deposit in the block was divided to the clusters proportionally to the energy deposits in the center block of each cluster.

The center (x) of the shower was calculated from two functions, X_0 and X_1, of the ratio of energy deposits in the adjacent blocks,

$$x=\pm X_1(E_{\pm 1}/E_0) \qquad \text{for } E_{+1}/E_0>0.2, \text{ or } E_{-1}/E_0>0.2\,, \tag{13.a}$$

and

$$x=X_0(E_{-1}/E_{+1}) \qquad \text{for the other case,} \tag{13.b}$$

where E_{-1}, E_0 and E_{+1} were the sums of the energies of three blocks in the same column or raw in the cluster as

$$E_i=\sum_i E_{i,j} \sum_j E_{j,i}\,, \qquad (i, j=-1, 0+1)\,. \tag{14}$$

The $E_{i,j}$ were energies of the blocks in the cluster and the indices i and j were column and raw numbers, respectively. The functions was obtained from a shower table which was made from the data of the electron calibration. The average shower profile is shown in fig. 13. After the position was determined, the energy of the cluster was corrected by using the shower table because some part of energy were deposited outside the cluster.

The mass was calculated for all combinations of a pair of clusters. Then a combination that gave the closest mass to the mass of π^0 was selected as a π^0 candidate. The energy of the combination was compared with the total energy deposit in the lead glass calorimeter. If the difference was large than the energy resolution, it was rejected as a multiple π^0 event.

The position resolution of π^0 was 2 mm (rms) obtained by the Monte-Carlo

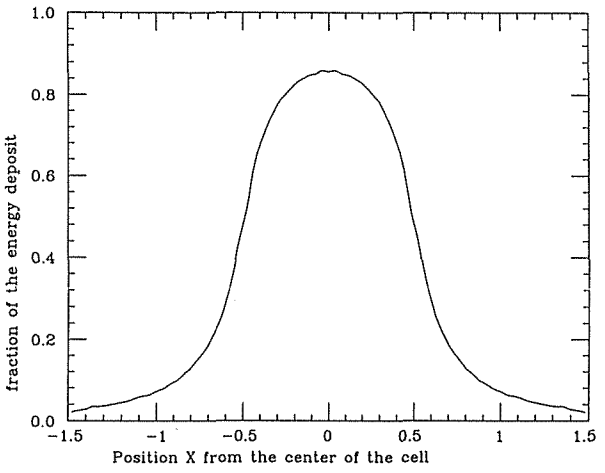

Figure 13 Fraction of the energy deposit in the block as a function of the shower position X, where $X=x$(cm)/size of the block (cm). It was deduced from the data of the calibration run.

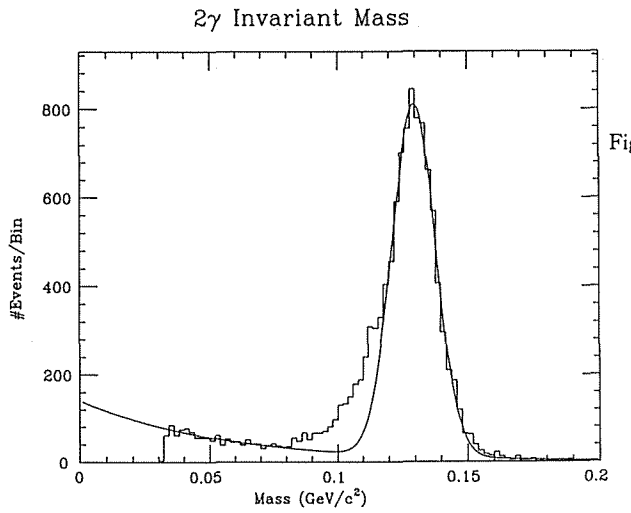

Figure 14 π^0 mass spectrum of the carbon data. The histogram is the data and the solid line is a sum of the exponential and gaussian functions which represent the background event and π^0, respectivelly. The π^0 peak was fitted for the $m_{\pi^0}=0.03 \sim 0.08$ GeV/c^2.

simulation. The mass spectrum of the reconstructed two γ's of the carbon data is shown in fig. 14. The width of the mass was 8.35 MeV/c^2 (rms). There was the tail in low mass side due to the leakage of the shower from the end and side walls. Some of these events were rejected by the fiducial cut on the photon positions later.

5.3 Event Selection for the Coherent Processes

The Coulomb coherent and diffractive processes have only one proton and one π^0 in the final state. Therefore the criteria of the event-selection were;

a) A single track with momentum from 100 to 160 GeV/c,
b) An interaction point within 50 cm from the target,
c) Two γ's mass between 0.117 GeV/c^2 and 0.150 GeV/c^2,
d) The reconstructed π^0 energy was equal to the total energy deposit in the lead glass calorimeter within the resolution,
e) The sum of the longitudinal momentum of the proton and π^0 was equal to the beam momentum within 10 GeV/c.

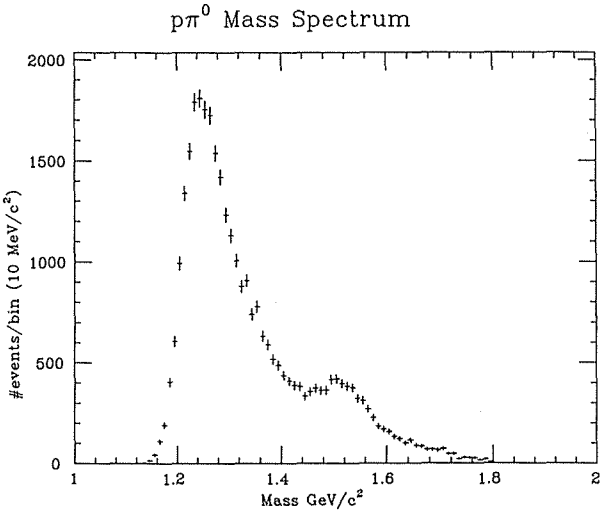

Figure 15 $p\pi^0$ mass spectrum of the lead data for $|t|<1\times10^{-3}$ $(\mathrm{GeV/c})^2$. Peaks of $\Delta(1232)$ and $N(1520)$ are seen clearly.

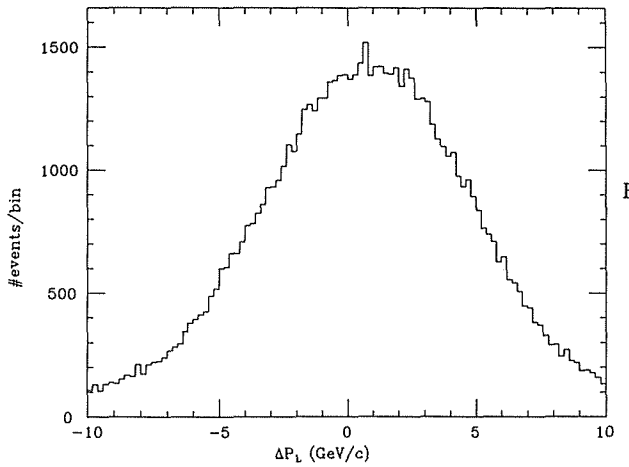

Figure 16 The distribution of the difference of the longitudinal momenta of the incident proton and $p\pi^0$.

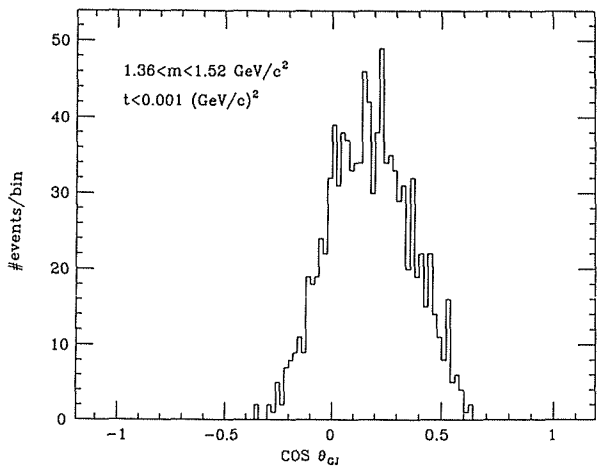

Figure 17 $\cos\theta_{\mathrm{GJ}}$ distribution of the coherent process for $t|<1\times10^{-3}$ $(\mathrm{GeV/c})^2$ and $m_{p\pi^0}=1.36\sim1.52\ \mathrm{GeV/c^2}$.

Above requirements were used to select the exclusive $p\pi^0$ events. The invariant mass spectrum of the $p\pi^0$ is shown in fig. 15. There are peaks of the $\Delta(1232)$ and $N(1520)$ resonances. The difference ΔP_L between longitudinal momenta of the incident proton and the final state ($p\pi^0$) is distributed around $\Delta P_L=0$ as shown in fig. 16. The width of the distribution is consistent with the momentum or energy resolutions of the beam, scattered proton and π^0. This shows that the selected events are the exclusive production of $p\pi^0$. The distribution of $\cos\theta_{G.J}$ for $t<1\times10^{-3}$ (GeV/c)^2 and $m_{p\pi^0}=1.36\sim1.52$ GeV/c^2 is also shown in fig. 17.

5.4 Asymmetry of the Coherent Process in Small $|t|$ Region

As described in Chapter 2, the cross section of the Coulomb coherent process for polarized protons is expressed in the form $(1+Ts_y)$, where T is the average of the target asymmetry $T(\theta')$ of the π^0-photoproduction in the acceptance of θ for the deterctor, and s_y is a spin component parallel to $\boldsymbol{n}=\boldsymbol{P}_B\times\boldsymbol{P}_p$ in the C.M.S. of the $p\pi^0$. Taking account of the presence of the background process, it is written as $1+rTs_y$, where r is a fraction of the Coulomb coherent process. Substituting s_y by $P\cos\phi$, where P is the beam polarization and ϕ is the angle between $\boldsymbol{n}$ and $\boldsymbol{S}=\boldsymbol{N}$ (upward vector) $\times\boldsymbol{L}$ (beam direction), the ϕ dependence of the cross section is expressed as $1+rTP\cos\phi$. The asymmetry ($\alpha=rTP$) of the coherent processes was deduced from the up-down asymmetry $A(\phi)$. The up-down asymmetry $A(\phi)$ is defined as

$$A(\phi)=[N_\uparrow(\phi)-N_\downarrow(\phi)]/[N_\uparrow(\phi)+N_\downarrow(\phi)], \tag{15}$$

where $N_\uparrow(\phi)$ and $N_\downarrow(\phi)$ are the ϕ-distributions for the upward and downward polarizations of protons, respectively. $N(\phi)$ can be fitted by the function

$$\alpha\cos(\phi). \tag{16}$$

The fit to the lead target data was performed for the $p\pi^0$ mass region of $1.36\sim1.52$ GeV/c^2, $|t|<1.0\times10^{-3}$ (GeV/c)^2 and for the tagged polarization between 0.35 and 0.65. The result was $\alpha=-0.14\pm0.03$ with $\chi^2=12.5$ and the number of degree of freedom (NDF) was 15. (fig. 18)

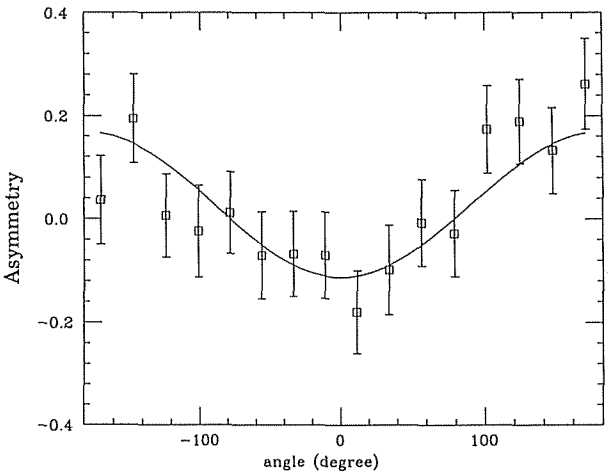

Figure 18 Asymmetry $A(\phi)$ for the lead target data. $t|<1\times10^{-3}$ (GeV/c)^2, $m_{p\pi^0}=1.36\sim1.52$ GeV/c^2.

The asymmetry in the region of the $p\pi^0$ mass$<1.36\,\mathrm{GeV/c^2}$ and $|t|<1.0\times10^{-3}$ $(\mathrm{GeV/c})^2$ was found to be -0.05 ± 0.017. Since the analyzing power in the region was close to zero as shown in fig. 3, the result indicates that there is no systematic asymmetry within the error of 0.017.

5.5 *t*-distribution

In order to obtain an asymmetry of the Coulomb coherent process, it must be separated from the background events. Since the t-dependence of the Coulomb coherent process and the diffractive process are different, the Coulomb coherent process could be separated from the diffractive process by fitting to t-distribution which is smeared by the P_T resolution. The background from air was estimated by using the empty-target data and it was subtracted from the lead target data.

5.5.1 Principle of Fitting to *t*-distribution

The t-dependence of the differential cross section of the Coulomb coherent process is

$$\frac{\mathrm{d}\sigma}{\mathrm{d}t}\propto\frac{t-t_0}{t^2}|F(t)|^2, \tag{18}$$

with $t_0=[\{(m_{p\pi^0})^2-(m_p)^2\}/2P_{p\pi^0}]^2$,

where $P_{p\pi^0}$ is the momentum of the $p\pi^0$ in the laboratory frame, $m_{p\pi^0}$ is the invariant mass of $p\pi^0$, and $F(t)$ is the nuclear form factor. Taking account of the t-resolution, $\Delta t=\Delta^2\sim(0.02\,\mathrm{GeV/c})^2$, the smeared t-distribution is obtained from the convolution integral

$$N_C(t)=C\int\mathrm{d}^2\bar{P}_T R(P_T,\bar{P}_T)\frac{\mathrm{d}\sigma}{\mathrm{d}\bar{t}}\,, \tag{19}$$

where $N_C(t)$ is the smeared t-distribution, the coefficient C is the conversion factor transforming from the cross section to an event rate. $R(P_T,\bar{P}_T)$ is the resolution function expressed as

$$R(P_T,\bar{P}_T)=\frac{1}{2\pi\Delta^2}\exp\{-\frac{R(P_T,\bar{P}_T)^2}{2\Delta^2}\}, \tag{20}$$

where $\bar{P}_T$ and P_T are the exact and smeared transverse momenta, respectively. $|t|=\bar{P}_T{}^2$, and Δ is the resolution of the transverse momentum P_T.[15,16] The integral in the equation (19) is evaluated numerically. The resulting t-distribution of the Coulomb coherent process behaves as $\exp(-bt)$ for $|t|<0.001$ $(\mathrm{GeV/c})^2$ and $|F(t)/|t|$ for $|t|>0.003$ $(\mathrm{GeV/c})^2$. The value of the slope parameter b approximately equals to $1/(2\Delta^2)\sim1000$ $(\mathrm{GeV/c})^2$. The t-distribution of the diffractive dissociation is also smeared in the same way, and it is expressed in an exponential form,

$$N_D(t)=D\exp(-b'_D t)\,, \tag{21}$$

with $b'_D=(1/b_D+2\Delta^2)^{-1}$,

where b_D is the slope parameter of the diffractive process, and the coefficient D includes a conversion factor similar to one in the equation (19). Therefore, the observed t-distribution $N(t)$ is the sum of the t-distributions of the Coulomb and diffractive processes as

$$N(t)=N_C(t)+N_D(t). \tag{22}$$

The t-distribution $N(t)$ dependes on the parameters, Δ, b_D and a ratio of the Coulomb to diffractive process.

5.5.2 Result of Fitting to t-distribution

The t-distribution of the lead target data after the background from the air was subtracted were fited by the equation (22). The t-distribution of the background was found to be 17.2 exp (-100t) for $m_{p\pi^0}=1.36\sim1.52$ GeV/c^2. The background from the air was estimated to be $2.5\pm0.5\%$ of the total events in the lead target data for $|t|<0.001$ (GeV/c)^2. The four parameters, Δ, b_D, C and D, were varied to achieve the best fit to the t-distribution for the $p\pi^0$ mass between 1.36 and 1.52 GeV/c^2 and $|t|=0.0\sim0.005$ (GeV/c)^2. (fig. 19(b)) The Δ, b_D and the fraction of the Coulomb coherent process, r, for $|t|<0.002$ (GeV/c)^2 are

$$\Delta=18.0\pm2.7 \text{ MeV/c},$$

$$b_D=508.1\pm30.0 \text{ (GeV/c)}^2,$$

$$r=0.537(+0.214/-0.144) \qquad \text{for } |t|<0.001 \text{ (GeV/c)}^2,$$

and $\chi^2=32.98$, NDF=47.

The P_T resolution Δ is consistent with the expected value within the error. The error in the ratio r came from the uncertainties of the P_T resolution Δ and the slope parameter b_D.

The results of fit to the t-distribution (fig. 19(a)) for the $p\pi^0$ mass less than 1.36 GeV/c^2 are

$$\Delta=16.0 \text{ MeV/c},$$

$$b_D=710.5\pm278 \text{ (GeV/c)}^2,$$

$$r=0.728\pm0.02,$$

and $\chi^2=63.16$, NDF=47.

The resolution Δ is smaller than one of the higher mass region since the transverse momenta of the proton and π^0 are smaller in the lower mass region than ones in the higher mass regions.

5.5.3 Study of Diffractive Process

The measurements with the carbon and copper targets were performed in order to understand the diffractive process (that was the main background process to the

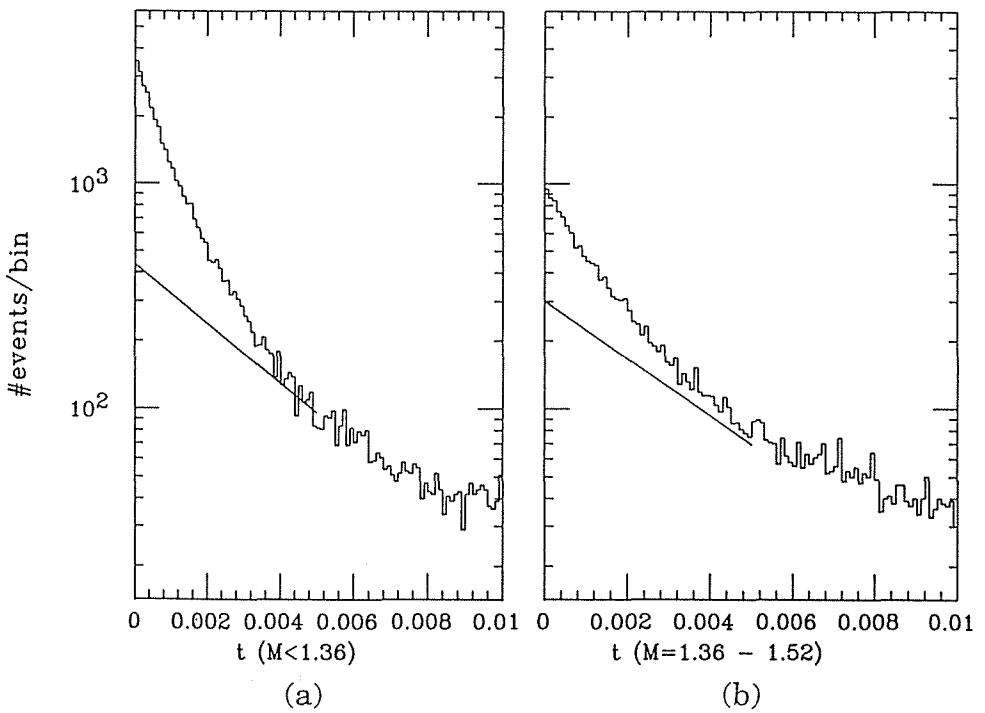

Figure 19 t-distributions of the lead target data for (a) $m_{\pi^0}<1.36$ GeV/c^2 and (b) $m_{p\pi^0}=1.36\sim 1.52$ GeV/c^2. The straight lines represent the diffractive process.

Coulomb coherent proccess). The t distributions in the various regions of the $p\pi^0$ mass were studied. The values of slope parameters were obtained by fitting the equation (22) to the carbon and copper data. The results of the fits to the carbon data are;

$$b_D=97.6\pm 9.4 \text{ (GeV/c)}^2 \text{ for } m_{p\pi^0}<1.36 \text{ GeV/c}^2,$$

$$b_D=77.7\pm 6.0 \text{ (GeV/c)}^2 \text{ for } m_{p\pi^0}=1.36\sim 1.52 \text{ GeV/c}^2.$$

The results of the fits to the copper data are;

$$b_D=242.9\pm 91.7 \text{ (GeV/c)}^2 \text{ for } m_{p\pi^0}<1.36 \text{ GeV/c}^2,$$

$$b_D=1721.1\pm 48.2 \text{ (GeV/c)}^2 \text{ for } m_{p\pi^0}=1.36\sim 1.52 \text{ GeV/c}^2.$$

The slope parameter b_D of the diffractive dissociation depends on the $p\pi^0$ mass. The slopes of the t distributions at low mass are larger than these at high mass. There are several theories to explain this behavior, such as a dual Deck model.[17-21] According to these theories, the value of slopes at high masses were determined by only the charge form factor of the nucleus, but the slopes at low masses were determined by the form factor of the nucleus and the vertex where the π^0 is produced. Empirically it is expressed as

$$R_{eff}=R_e+R_I m^{-1}, \tag{23.a}$$

$$b_D = R_{eff}^2/4, \tag{23.b}$$

where R_e is the nuclear radius obtained from electron scattering and R_I is an interaction radius, $R_I \sim 1$ fm, and m is the $p\pi^0$ mass. The radii and slope parameters in the case of carbon and copper are;[29]

$$Cu: R_e = 3.24 \pm 0.10 \text{ fm}, \quad b_D = 65.6 \sim 112.4 \text{ (GeV/c)}^2,$$
$$Cu: R_e = 5.60 \pm 0.10 \text{ fm}, \quad b_D = 196.0 \sim 272.3 \text{ (GeV/c)}^{-2},$$

where the slope parameters b_D are for $m_{p\pi^0} = 1.1 \sim 1.8$ GeV/c^2. The slope parameters of carbon and copper are consistent with our data. Therefore, the slope parameter for the lead target is estimated to be 350~460 (GeV/c)^2, and it is slightly smaller than our data described in the previous section.

6 Results and Discussion

The polarization of the polarized proton beam at FNAL has been measured by making use of the asymmetry of the Coulomb coherent production. The energy of the polarized beam was 185 ± 11 GeV. The measured asymmetry for the lead target is 0.14 ± 0.03 in the $p\pi^0$ mass region of 1.36~1.52 GeV/c^2, the angular range of 60~105 degrees in θ_{GJ}, and t of less than 1×10^{-3} (GeV/c)^2. The fraction of the Coulomb coherent process in this kinematical region was found to be 0.539 ($+0.214/-0.144$). The results are compared with the data on the asymmetry of π^0-photoproduction on the polarized proton target at low energies. The average asymmetry of π^0-photoproduction in the same mass region is 0.65 ± 0.04. The polarization of the beam was found to be 0.4 ± 0.09. The asymmetries in the different kinematical regions were also obtained, in order to test the systematical asymmetry in the measurements. In the same angular and t ranges and in the lower $p\pi^0$ mass range of 1.2~1.36 GeV/c^2, the asymmetry was found to be -0.005 ± 0.017. It is consistent with the average asymmetry of the π^0-photoproduction. The asymmetry in the range of $0.0025 \times 10^{-3} \sim 0.005 \times 10^{-3}$ (GeV/c)^2 and the $p\pi^0$ mass region of 1.36~1.52 GeV/c^2 was found to be 0.012 ± 0.028. As a result, the nuclear diffractive process has no analyzing power because the nuclear diffractive process dominated in this region. It is expected to have no analyzing power event at $t=0$. This also indicats that there is no systematic asymmetry of the measurement.

It is proved that the Coulomb coherent production has the asymmetry given by the equation (12) based on the target asymmetry of the low-energy π^0 photoproduction. Because the analyzing power is independent of the beam energy according to the equation (12), this process is quite useful to measure the polarization of protons at high energies with a small uncertainty.

The beam polarization was measured by the proton-proton elastic scattering in the Coulomb nuclear interference (CNI) region[14] just after our measurement using the same polarized beam. The p-p scattering shows that the beam polarization is $41 \pm 25\%$, which is consistent with our results within the statistical errors. The beam polarization was also evaluated to be about 45% from the decay asymmetry of Λ^0 using the data on the

beam tagging. The value is also in good agreement with ours.

Using the polarized beam described in this paper, the analyzing power of the inclusive π^0 production in $p+p$ collision in large-x_F was measured, and was found to be 10% in the region of $0.2<x_F<0.8$ and $0.3<P_T<1.2$ GeV/c at the incident energy of 185 GeV.[28]

Acknowledgements

The execution of the experiment described in this paper has been a combined effort of many individuals in E-704 collaboration. The collaborators in this experiments were: K. Imai, A. Konaka, S. Makino, A. Masaike, K. Miyake, T. Nakano, N. Tamura, T. Yohsida from Kyoto University, F. Takeushi from Kyoto Sangyo University, R. Takashima from Kyoto University of Education, T. Maki from University of Occupational and Environmental Helth, D. P. Grosnick, D. A. Hill, D. Lopiano, Y. Ohashi, T. Shima, H. M. Spinka, R. W. Stanek, D. G. Underwood, A. Yokosawa from Argonne National Laboratory, D. C, Carey, R. N. Coleman, J. D. Cossairt, A. L. Read from Fermilab, A. A. Derevshchikov, A. P. Meshchanin, Yu. A. Matulenko, S. B. Nurushev, V. L. Solovyanov, A. N. Vasiliev from IHEP Serukhov, L. van Rossum, F. Lehar, A. de Lesquen from CEN-Saclay, K. Kuroda, A. Michalowitz from LAPP, F. C. Leuhring, D. H. Miller from Northwestern University, G. Pauletta from University of Udine, A. Penzo, G. Salvato, A. Villari, A. Zanetti from University of Trieste, B. E. Bonner, J. A. Buchanan, J. W. Kruk, H. E. Miettinen, J. M. Clement, M. D. Corcoran, A. H. Mohammadzadeh, G. S. Mutchler, F. Nessi-Tedaldi, M. Nessi, C. Nguyen, G. C. Philips, J. B. Roberts, P. Schiavon, P. M. Stevenson, J. L. White, and Q. Zhu from Rice University.

I wish to thank all of the people at Fermilab who have constructed this special beam line that was essentially needed to our experiment. I thank for advice and guidance from Professors A. Masaike, K. Miyake and K. Imai. I am grateful for very careful advice from Dr. D. G. Underwood. I also thank to Prof. T. Nakamura and Dr. N. Sasao, Y. Henmi and R. Kikuchi for their encouragement. It was useful and pleasure to discuss with Drs. S. Kunori, T. Yamanaka and N. Oshima.

References

1 J. Antille et al., Phys. Lett. **94B**, 523 (1989).
2 V. D. Apokin et al., Asymetry in the Inclusive Reaction $pi \to pi0 + x$ at high pt at 40 GeV/c, the proceedings of The VII International Symposium on High Energy Spin Physics, Protvino, USSR, Vol. 2, 83 (1986).
3 D. G. Underwood, AIP Conf. Proc. **176**, 1118 (1988).
4 R. N. Coleman, Proc. of the Symposium on Future Polarization Physics at Fermilab, p. 55 (1988).
5 H. Primakoff, Phys. Rev. **81**, 899 (1951).
6 A. Halprin, C. M. Anderson and H. Primakoff, Phys. Rev. **152**, 1295 (1966).
7 D. G. Underwood, ANL-HEP-PR-77-56.
8 K. Kuroda, AIP Conf. Proc. **95**, 618 (1982).
9 B. Margolis and G. H. Thomas, AIP Conf. Proc. **42**, 173 (1978).
10 R. L. Walker, Phys. Rev. **182**, 1729 (1969).

11 K. Ukai and T. Nakamura, INS-TEC-22.
12 M. Fukishima et al., NP **B136**, 189 (1978).
13 M. Yoshioka et al., Nuclear Physics **B168**, 222 (1980).
14 G. Pauletta, TESTS OF COULOMB-NUCLEAR POLARIMETER, Proceedings of High Energy Spin Physics 1988 (to be published).
15 T. Jensen et al., Phys. Rev. **D27**, 26 (1983).
16 T. Jensen, MEASUREMENT OF THE RADIATIVE DECAY WIDTH OF THE ROH MESON, PhD Thesis, The University of Rochester, 1980.
17 T. Oshima, private communiation.
18 G. Alberi and G. Goggi, Physics Reports **74**, 1 (1981).
19 S. D. Drell and K. Hiida, Phys. Rev. Lett. **7**, 199 (1961).
20 F. F. Deck, Phys. Rev. Lett. **13**, 169 (1964).
21 M. Ross and Y. Y. Yam, Phys. Rev. Lett. **19**, 546 (1967).
22 J. W. Cronin and O. E. Overseth, Phys. Rev. **129**, 1795 (1963).
23 O. E. Overseth, Phys. Rev. Lett. **81**, 391 (1967).
24 D. G. Underwood, NIM **173**, 351 (1980).
25 T. Homma et al., Japan J. Appl. Phys. **26**, 602 (1987)
26 J. Lindsay et al., A general purpose amplifier and read-out system for multiwire proportional chambers, CERN 74–12 (1974).
27 G. Bellettini et al., NP **79**, 609 (1966).
28 B. E. Bonner, et al. (FNAL-E704 Collaboration), Phys. Rev. Lett. **61**, 1918 (1988).